



Fabrication of $\text{In}_2\text{O}_3/\text{In}_2\text{S}_3$ microsphere heterostructures for efficient and stable photocatalytic nitrogen fixation

Huichang Xu, Yu Wang*, Xiaoli Dong*, Nan Zheng, Hongchao Ma, Xiufang Zhang

School of Light Industry and Chemical Engineering, Dalian Polytechnic University, #1 Qinggongyuan, Dalian 116034, PR China

ARTICLE INFO

Keywords:

$\text{In}_2\text{O}_3/\text{In}_2\text{S}_3$ heterostructures
Microsphere
Photocatalytic nitrogen fixation

ABSTRACT

The synthesis of a novel $\text{In}_2\text{O}_3/\text{In}_2\text{S}_3$ microsphere heterostructures is conducted through a well-designed two-step hydrothermal method. These composites are first applied for efficient fixation of N_2 to NH_3 under mild conditions without any organic scavengers and precious-metal cocatalysts. Here the In_2S_3 flakes are in situ generated and uniformly assembled on In_2O_3 microsphere. The phase structures, morphologies and oxygen vacancies of the samples are systematically characterized by X-ray powder diffraction (XRD), field-emission scanning electron microscopy (SEM), transmission electron microscopy (TEM), X-ray photoelectron spectroscopy (XPS), UV-vis diffuse-reflectance spectroscopy (DRS), and photoluminescence spectroscopy (PL), Raman, electron spin resonance (ESR) spectroscopy and photoelectrochemistry. Meanwhile, the investigation of photocatalytic performance can confirm that the nitrogen fixation rate of $\text{In}_2\text{O}_3/\text{In}_2\text{S}_3$ (III) heterostructure is $40.04 \mu\text{mol g}^{-1} \text{h}^{-1}$, which is about 4.7 and 6.0 times higher than that of pure In_2O_3 and In_2S_3 , respectively.

1. Introduction

As we known, nitrogen plays an important role in the development of human society, which is a significant component of protein to construct the essence in life [1]. Ammonia with the great hydrogen storage capacity is studied extensively owing to its high hydrogen density and low liquefying pressure [2,3]. N_2 , accounting for 78% of the total volume of the atmosphere, is the most abundant gas on the earth. Hence, the research on converting N_2 to NH_3 has attracted considerable attention. In 1910, Haber-Bosch process applied N_2 and H_2 to generate ammonia, which greatly promoted the progress of industrial fixation of N_2 to NH_3 . However, the method required drastic conditions, mainly manifesting in temperature (400–600 °C) and pressure (20–40 MPa) [4,5], which could cause great consume of fossil fuels and then a series of climate problems. In view of the above-mentioned facts, the issue on utilizing light energy into artificial nitrogen fixation under mild conditions currently attracts intense interest in fundamental studies and applications [6].

On the basis of the previous studies, nitrogen molecules exhibit chemical inertia due to the extraordinarily large dissociation energy (410 kJ mol^{-1}) of the first chemical bond, which can block the cleavage and hydrogenation of nitrogen [7,8]. Furthermore, the energy gap between the highest occupied molecular orbital (HOMO) and lowest unoccupied molecular orbital (LUMO) is extremely large to hinder

nitrogen molecules to become more energetic, so it is barely for nitrogen to conduct some chemical reactions [9]. In recent years, the studies have been carried out and achieved a series of developments in photocatalytic nitrogen fixation under gentle conditions. The photo-generated electrons of photocatalysts will be excited when the semiconductor directly captures the energy from sunlight. Meanwhile, the holes produced in the valence band (VB) can oxidize H_2O to O_2 , and incidentally N_2 will be reduced to NH_3 by the activated electron generated in the conduction band (CB) [10]. Because of the poor interfacial charge transfer, the results of photocatalytic nitrogen fixation are far from satisfied [11–13]. To promote its application in photocatalytic nitrogen fixation fields, good charge/mass-transfer ability is also required to facilitate the catalytic kinetics [14]. At the moment, studies devote to ameliorating the photocatalytic performance in nitrogen fixation, such as BiOBr nanosheets [1], g- C_3N_4 nanosheets [15], $\text{Mo}/\text{W}_{18}\text{O}_{49}$ [16].

Owing to the outstanding conductivity and thermodynamic stability [17–19], indium (III) oxide (In_2O_3), an n-type semiconductor photocatalyst with the band gap of 2.8 eV [20], has captured much attention in photoelectrochemistry [21], chemical sensors [22], photocatalytic hydrogen generation [23] and the degradation of organic pollutants [24]. However, previous studies have not reported the application in photocatalytic nitrogen fixation. More recently, some results have indicated that the In_2O_3 usually exhibits poor photocatalytic performance

* Corresponding authors.

E-mail addresses: wang_yu@dlpu.edu.cn (Y. Wang), dongxiaoli65@163.com (X. Dong).

<https://doi.org/10.1016/j.apcatb.2019.117932>

Received 7 April 2019; Received in revised form 17 June 2019; Accepted 6 July 2019

Available online 08 July 2019

0926-3373/ © 2019 Elsevier B.V. All rights reserved.

because of the high recombination rate of photoexcited electrons and holes and the low utilization of photon of solar spectrum [25]. Thus, some new attempts would be committed to improving photocatalytic property by forming heterojunctions at the interface with other materials [26,27]. Among them, indium sulfide (In_2S_3), a typical III–VI group sulfide with visible-light activities, has been reported lately [28,29]. It possesses three different polymorphic forms: α - In_2S_3 , β - In_2S_3 and γ - In_2S_3 . β - In_2S_3 , an n-type semiconductor with a narrow bandgap of 2.0–2.3 eV, has been extensively applied due to its high photosensitivity and photoconductivity, chemical stability and high utilization of light energy [30–32]. To date, many $\text{In}_2\text{O}_3/\text{In}_2\text{S}_3$ composites had been manufactured and used in photocatalytic field. For instance, Hou et al. reported that an $\text{In}_2\text{O}_{3-x}/\text{In}_2\text{S}_3$ lateral heterostructure displayed superior performance in water splitting than pure In_2O_3 or In_2S_3 [33]. Yang et al. composed inverted type-I $\text{In}_2\text{O}_3/\text{In}_2\text{S}_3$ core-shell nanorods, which exhibited excellent efficiency in H_2 evolution under mild conditions [34]. Chen et al. recently showed that by using 3D $\text{In}_2\text{O}_3/\text{In}_2\text{S}_3$ microflowers, the effect of photocatalytic degradation of gaseous ortho-dichlorobenzene can be promoted enormously [35].

Here we reported the synthesis of $\text{In}_2\text{O}_3/\text{In}_2\text{S}_3$ heterostructure via an efficient and simple two-step hydrothermal approach. In_2O_3 microsphere was prepared during the first hydrothermal process, and then the In_2S_3 flower slices were generated on microsphere structure via a subsequent in situ anion exchange process after second hydrothermal process. Next, technical methods were adopted to investigate the microstructures, photochemical and photophysical properties, oxygen vacancies and specific surface area of the $\text{In}_2\text{O}_3/\text{In}_2\text{S}_3$ composites. The as-synthesized materials with the perfect interfacial contact showed high UV–vis light activities and efficient charge separation than that of pure In_2O_3 and In_2S_3 . Subsequently, the nitrogen fixation performance of the material was manifested by spectrophotometrically measuring with Nessler's reagent. Especially, there has been no report on applying $\text{In}_2\text{O}_3/\text{In}_2\text{S}_3$ heterostructures in the photocatalytic nitrogen fixation. Our study provided an environmentally-friendly and mild chemical route to nitrogen fixation by using In_2O_3 -based photocatalysts.

2. Experimental section

2.1. Chemicals and materials

Indium chloride tetrahydrate ($\text{InCl}_3 \cdot 4\text{H}_2\text{O}$, 99.9% metals basis) was purchased from Aladdin Industrial Corporation. Sodium dodecylsulfate (SDS, $\text{C}_{12}\text{H}_{25}\text{NaO}_4\text{S}$, 97.0%) was supplied by Xilong Scientific Co., Ltd.. Urea ($\text{CO}(\text{NH}_2)_2$, 99.0%) and Nessler's reagent was purchased from Tianjin Damao Chemical Reagent Co., Ltd.. Thioacetamide (TAA, CH_3CSNH_2 , 99.0%) was supplied by Tianjin Guangfu Chemical Reagent Co., Ltd. and absolute ethanol (EtOH , 99.7%) was obtained from Tianjin Fuyu Fine Chemical CO., Ltd.

2.2. Preparation of In_2O_3 and $\text{In}_2\text{O}_3/\text{In}_2\text{S}_3$ microsphere heterostructures

The chemical reagents except SDS used in this study were of analytical pure grades, and SDS was chemical pure grades. They were not further purified. In this work, the $\text{In}_2\text{O}_3/\text{In}_2\text{S}_3$ heterostructures were synthesized by a facile two-step hydrothermal method. Firstly, the 0.9 mmol of $\text{InCl}_3 \cdot 4\text{H}_2\text{O}$, 2.8 mmol of SDS and 4.7 mmol of urea were added to 80 mL deionized water under vigorous magnetically stirring for 1 h, and then the mixture was poured into a Teflon-lined stainless-steel autoclave and heated at 120 °C for 12 h. In the next moment, the autoclave was cooled to room temperature and then the product was washed many times by deionized water and absolute ethanol alternately. Finally the white powder was collected and dried at 60 °C for 12 h. The light yellow In_2O_3 powder was obtained after calcining the white product at 500 °C for 2 h in air. Next, 0.1 g of In_2O_3 powder prepared in previous step was added into 30 mL deionized water, and stirred for 30 min to form uniform suspension. Different amount (0.03,

0.04, 0.05, 0.06 and 0.1 g) of thioacetamide (TAA) were put into the suspension with stirring continuously for 1 h, and then the suspensions were transferred to a 40 mL Teflon-lined stainless-steel autoclave and kept at 150 °C for 5 h. After the autoclave cooled down, the final precipitates were collected by centrifugation after washing alternately with deionized water and absolute alcohol several times, and dried at 60 °C. A series of $\text{In}_2\text{O}_3/\text{In}_2\text{S}_3$ heterostructures were synthesized and defined as $\text{In}_2\text{O}_3/\text{In}_2\text{S}_3$ (X, X = I, II, III, IV) heterostructures, which represent the dosages of TAA were 0.03, 0.04, 0.05 and 0.06 g, respectively.

2.3. Characterization

The powder X-ray diffraction (XRD) patterns of the samples were measured in the degree range of 20–80 by using a Shimadzu XRD-6100 diffractometer with Cu K α radiation ($\lambda = 0.145$ nm) at 40 kV and 100 Ma. The micromorphology and elemental composition information of the material were obtained by the scanning electron microscope (SEM, JEOL, JSM-7800 F) with an EDS detector and transmission electron microscope (TEM, JEOL JEM-2000EX). X-ray photoelectron spectroscopy (XPS) spectra were investigated on a VG Scientific ESCALAB250 XPS instrument. The light absorption spectra were recorded by using UV–vis diffuse reflectance spectra (DRS, CARY 100 CONC spectrometer). The relative concentration of oxygen vacancies was performed with an ESR spectrometer A200 (Bruker, Karlsruhe, Germany) at room temperature. The surface area was carried out by nitrogen adsorption–desorption using Quantachrome NOVA 2000 at 77 K. Then the amount of O_2 and NO_3^- in sealed reactor were determined by gas chromatography (Shiweipx GC7806) and ion chromatograph (Thermo Dionex ICS-5000).

Photoelectrochemical (PEC) measurements were performed on a CHI760E electrochemical workstation (Shanghai Chenhua, P. R. China) with a three-electrode configuration. A Pt plate was used as counter electrode, and the Ag/AgCl was as the reference electrode. The working electrode was prepared using 10 mg as-prepared sample suspended in the mixture of 10 μL Nafion solution (D520, DuPont), 1.5 mL ethanol and 0.5 mL ultrapure water, which was then dip-coated onto a glass carbon electrode and dried in the shade. The electrolyte was an aqueous solution of 0.5 M Na_2SO_4 . The 300 W Xenon lamp (PLS-SXE 300, Beijing Perfect Light Co., Ltd.) was used as the light source. The photocurrent response was obtained by potentiostatic (current vs. time, I-t) measurements under intermittent illumination (30 s) in the condition of no bias potential.

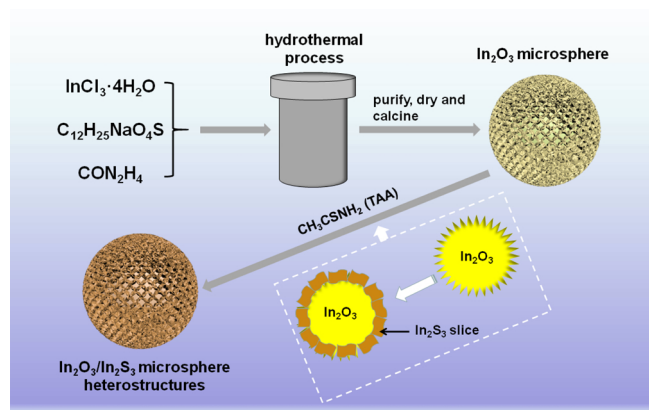
2.4. Photocatalytic N_2 fixation activity test

All the experiments of nitrogen fixation performance were carried out under ambient conditions. In the experiment, we used 300 W Xenon lamp without filter as light source. The height from the light source to the surface of liquid was about 10 cm, and the light intensity was 200 W/cm². Firstly, 0.02 g photocatalyst and 100 mL deionized water were added into the reactor, and the photocatalyst was dispersed to form uniform suspension via sonication for 5 min. Secondly, a circulating water system was connected to the reactor in order to keep the reaction environment at 15 °C. With continuously stirring, high-purity nitrogen was bubbled into the reactor at the flow rate of 80 mL/min, the mixture was reacted in darkness for 30 min, and then reacted under light irradiation. 5 mL portions of the suspension was withdrawn per 30 min and the liquid sample was filtered through 0.22 μm filter to remove the photocatalyst. Nessler's reagent was used as chromogenic agent, and the concentration of NH_4^+ was detected at 420 nm in the spectrophotometer.

3. Results and discussion

3.1. Results of characterization

The $\text{In}_2\text{O}_3/\text{In}_2\text{S}_3$ microsphere heterostructures are prepared via a



Scheme 1. Schematic diagram of the synthetic route for $\text{In}_2\text{O}_3/\text{In}_2\text{S}_3$ microsphere heterostructures.

two-step hydrothermal approach (Scheme 1). Fig. 1 shows the XRD diagrams of pure In_2O_3 , In_2S_3 and $\text{In}_2\text{O}_3/\text{In}_2\text{S}_3$ (I II III IV) heterostructures. It can be observed that the broad diffraction peaks of pure In_2O_3 located at 30.8° , 35.5° , 51.5° and 60.8° are identical to bcc- In_2O_3 (JCPDS No. 06-0416). The pattern of $\beta\text{-In}_2\text{S}_3$ has a large number of peaks well-indexed to JCPDS No. 65-0459. Furthermore, the diffraction peaks of the $\text{In}_2\text{O}_3/\text{In}_2\text{S}_3$ heterostructures also show the similar XRD patterns to those of bcc- In_2O_3 and $\beta\text{-In}_2\text{S}_3$. The diffraction peaks of $\beta\text{-In}_2\text{S}_3$ gradually become stronger with the increasing amount of sulfur source, meanwhile, the bcc- In_2O_3 diffraction peaks are obviously weakened. When the dosages of TAA is increased to 0.1 g, the characteristic peaks at 27.7° , 33.5° , 43.8° and 47.9° can be indexed to the (311), (400), (511) and (440) crystal phases of $\beta\text{-In}_2\text{S}_3$. In the whole process of experiment, no other impurity phase is observed.

In order to further characterize the structures of pure In_2O_3 , In_2S_3 and $\text{In}_2\text{O}_3/\text{In}_2\text{S}_3$ (I II III IV) heterostructures, SEM images are displayed in Fig. 2. Pure In_2O_3 exhibits the structure similar to microsphere with diameter between $1\text{--}2\mu\text{m}$, which is composed of the thin and dense slices on the surface. When adding different amounts of sulfur source, as shown in Fig. 2c–g, the phenomenon that In_2S_3 slices grow uniformly on the surface of In_2O_3 microsphere is verified after the second hydrothermal treatment. In addition, the number densities of the In_2S_3 slices gradually increase with the augment of TAA content. Typically, Fig. 2h shows the slices of pure In_2O_3 couldn't be observed when the amount of TAA reaches 0.1 g. Furthermore, the element-mapping images of $\text{In}_2\text{O}_3/\text{In}_2\text{S}_3$ (III) heterostructure (Fig. 2i) reveal that all elements are uniformly distributed in the final product.

The detailed crystalline information of the as-prepared materials

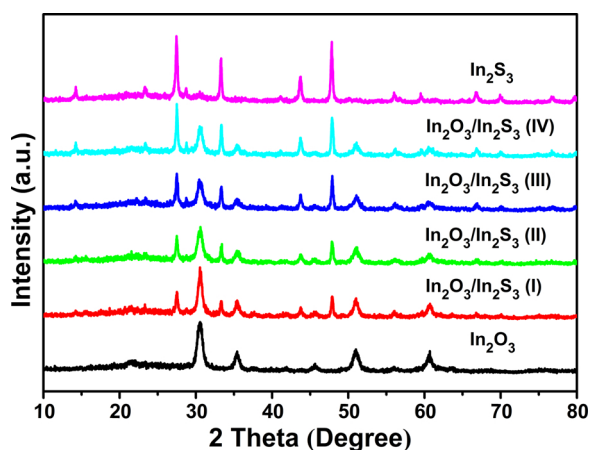


Fig. 1. XRD patterns of pure In_2O_3 , In_2S_3 and $\text{In}_2\text{O}_3/\text{In}_2\text{S}_3$ (I II III IV) heterostructures.

has been obtained through the TEM images. Fig. 3a presents that the TEM image of In_2O_3 microsphere on which the slices are relatively thin and smooth. However, the TEM diagram of $\text{In}_2\text{O}_3/\text{In}_2\text{S}_3$ (III) heterostructure performs thicker layer after vulcanization, and the border of materials becomes gradually clear. Fig. 3c shows the slices of In_2O_3 disappear when the dosage of TAA becomes 0.1 g. The morphology and more details of phase information of $\text{In}_2\text{O}_3/\text{In}_2\text{S}_3$ (III) heterostructure are shown in HRTEM image (Fig. 3d). It can be found that there are two lattices with the interfringe spacings of 0.294 and 0.272 nm, matching well with the (222) and (400) crystal of In_2O_3 and In_2S_3 .

The optical absorption performance is a key factor to test the photocatalytic properties of semiconductor, and it can be characterized by UV–vis absorption spectra. As shown in Fig. 4a, the strong absorption of the pale yellow In_2O_3 at less than 500 nm indicates that scope of absorption light is mostly in ultraviolet region, consisting with previous literature [36]. As the quantity of sulfur source gradually increasing, the absorption peaks gradually move to visible light area. Specially, the red shift of absorption band edge is distinctly observed in $\text{In}_2\text{O}_3/\text{In}_2\text{S}_3$ (III) heterostructure, and the intensity of the absorption peaks also increases greatly. In brief, the formation of In_2S_3 sheets can effectively change the optical absorption of materials, resulting in the enhanced photocatalytic performance of materials.

The changes of band gap energies (E_g) can be reflected by a Kubelka-Munk function. According to previous reports [37–39], the band gap energies can be calculated by the Eq. (1):

$$A\hbar\nu = k(\hbar\nu - E_g)^{n/2} \quad (1)$$

where α stands for the absorption coefficient, h and ν are the Planck constant and light frequency respectively, k is a constant and the band gap energy can be represented by E_g , for the semiconductor with direct band gap, the n is 1. The final calculated result are shown in Fig. 4b. The E_g values of pure In_2O_3 , In_2S_3 and $\text{In}_2\text{O}_3/\text{In}_2\text{S}_3$ (I II III IV) heterostructures are 2.77, 2.01, 2.09, 2.11, 2.04 and 2.02 eV, which indicate that the heterojunctions have lower band gap energy and higher utilization rate of protons after the surface sulfuration.

In fact, O-vacancies can play the role of trapping photon-generated electrons as active sites of semiconductor photocatalyst [40]. According to previous reports, when $\text{In}(\text{OH})_3$ is calcined to form In_2O_3 , the oxygen in the hydroxyl species will be released to form oxygen vacancies. Besides, in the process of in situ anion exchange process by sulfuration, the lattice oxygen of In_2O_3 will also be released to form O_2 , thus more oxygen vacancies can be further formed in the materials [41,42]. It is well known that oxygen vacancies, as an important factor, can affect semiconductor photocatalytic performance by extending the range of light response and improving the separation efficiency of photo-generated electrons and holes [43]. To further characterize the concentration of oxygen vacancies in the materials, ESR detections are conducted. As shown in Fig. 5a, the samples of pure In_2O_3 , $\text{In}_2\text{O}_3/\text{In}_2\text{S}_3$ (III) heterostructure and In_2S_3 exhibit obvious ESR signals at $g = 2.002$, which is consistent with the typical signal of oxygen vacancies. Compared with the pure In_2O_3 and In_2S_3 sample, the ESR signal peak of $\text{In}_2\text{O}_3/\text{In}_2\text{S}_3$ (III) heterostructure possesses the highest intensity in the all materials.

The oxygen vacancies can also be detected by the Raman spectra. As shown in Fig. 5b, several distinct characteristic peaks appear at 132, 309, 368, 498 and 630 cm^{-1} , assigned to the presence of bcc- In_2O_3 . Among them, the Raman peaks at 132 and 368 cm^{-1} represent the In-O vibration of InO_6 structure units and the stretching vibration of In-O-In linkages [35,44], respectively. The strength ratio between 132 and 368 cm^{-1} can further indicates the oxygen vacancies content. Obviously, the value of strength ratio in $\text{In}_2\text{O}_3/\text{In}_2\text{S}_3$ (III) heterostructure is higher than that of pure In_2O_3 , indicating that the oxygen vacancies are generated from the lattice oxygen, and the result is consistent with that of ESR.

The XPS spectra can be used to reveal the information of chemical

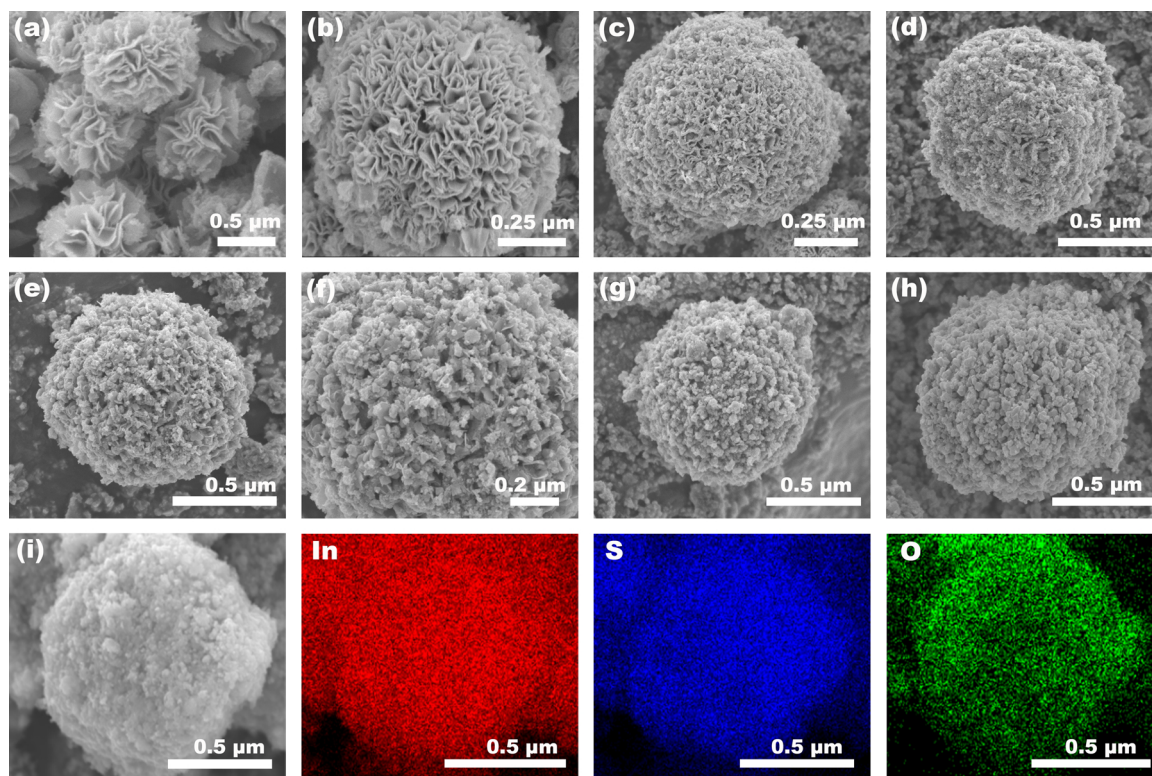


Fig. 2. SEM images of (a) and (b) In_2O_3 . (c) $\text{In}_2\text{O}_3/\text{In}_2\text{S}_3$ (I) heterostructure. (d) $\text{In}_2\text{O}_3/\text{In}_2\text{S}_3$ (II) heterostructure. (e) $\text{In}_2\text{O}_3/\text{In}_2\text{S}_3$ (III) heterostructure. (f) The surface of $\text{In}_2\text{O}_3/\text{In}_2\text{S}_3$ (III) heterostructure. (g) $\text{In}_2\text{O}_3/\text{In}_2\text{S}_3$ (IV) heterostructure. (h) In_2S_3 . (i) The elemental mapping image of In, O and S in the $\text{In}_2\text{O}_3/\text{In}_2\text{S}_3$ (III) heterostructure.

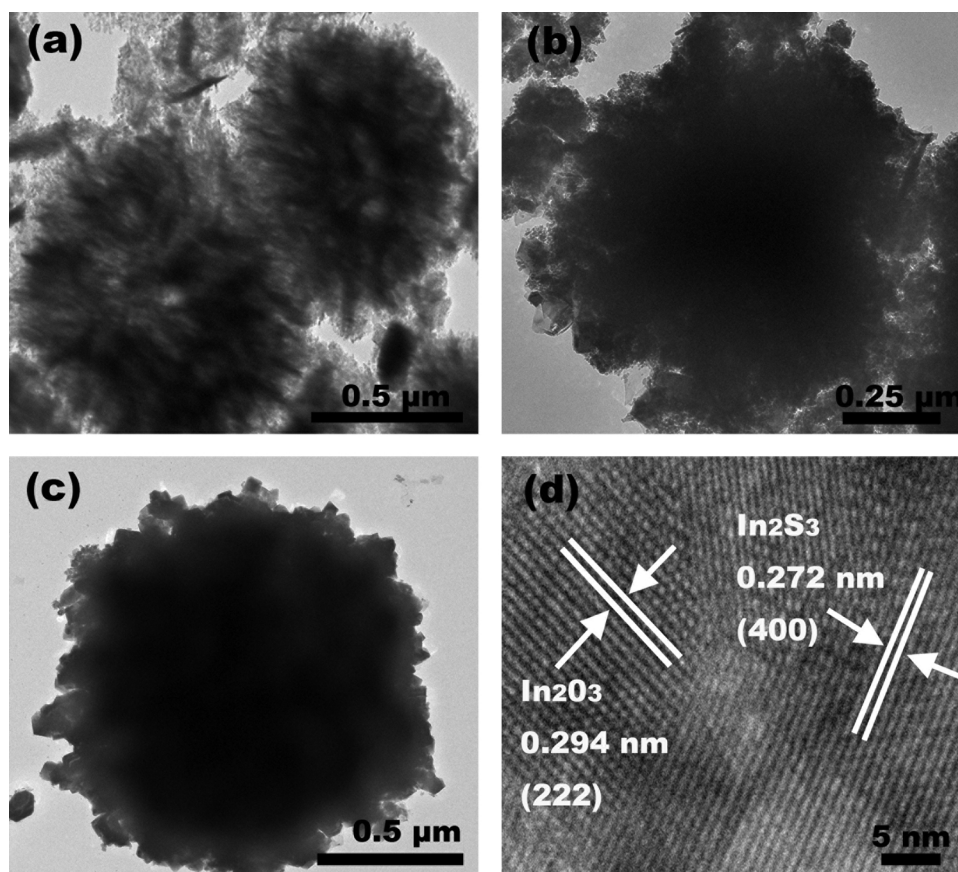


Fig. 3. TEM images of (a) pure In_2O_3 , (b) $\text{In}_2\text{O}_3/\text{In}_2\text{S}_3$ (III) heterostructure, (c) In_2S_3 and HRTEM (d) image of $\text{In}_2\text{O}_3/\text{In}_2\text{S}_3$ (III) heterostructure.

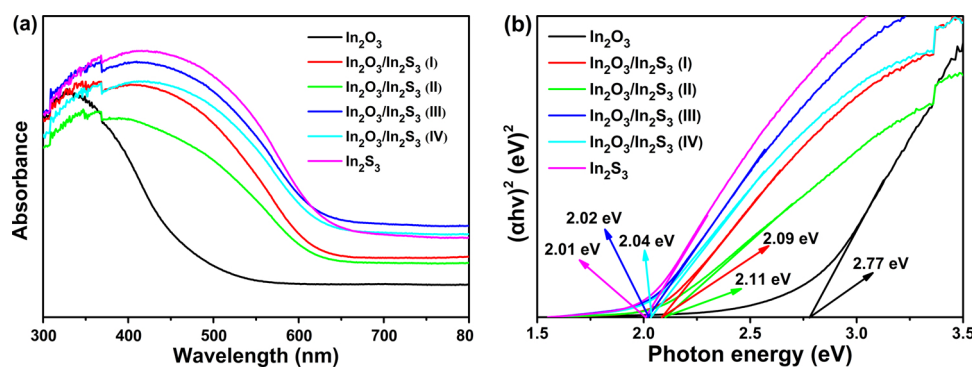


Fig. 4. (a) UV-vis absorption spectra profiles. (b) The plot of $(\alpha h\nu)^2$ versus photo energy ($h\nu$) of pure In_2O_3 , In_2S_3 and $\text{In}_2\text{O}_3/\text{In}_2\text{S}_3$ (I II III IV) heterostructures.

composition of the as-prepared samples. Fig. 6a presents the survey spectrum of the $\text{In}_2\text{O}_3/\text{In}_2\text{S}_3$ (III) heterostructure sample, demonstrating the co-existence of In, O and S elements. As shown in Fig. 6b, the XPS spectrum of In 3d for pure In_2O_3 shows two obviously prominent peaks with binding energies of approximately 444.4 eV and 451.9 eV, which could be assigned to $\text{In } 3d_{5/2}$ and $\text{In } 3d_{3/2}$, respectively. However, after the incorporation of In_2S_3 slices, the location of binding energies shifts to the higher value. The S 2p spectrum of pure In_2S_3 is shown in Fig. 6c. The two peaks of binding energies, located at 162.5 eV and 161.4 eV, are attributed to $\text{S } 2p_{1/2}$ and $\text{S } 2p_{3/2}$, while the lower binding energies appear with the formation of $\text{In}_2\text{O}_3/\text{In}_2\text{S}_3$ heterostructures. Those shifts of binding energies indicate that the emergence of heterojunctions affects the chemical environment between In_2O_3 and In_2S_3 , and the electronic interaction is important to the transfer of photogenerated carriers [35]. To resolve the valence states of oxygen element, the O 1s XPS spectra of pure In_2O_3 and $\text{In}_2\text{O}_3/\text{In}_2\text{S}_3$ (III) heterostructure are collected. Two asymmetric peaks of O 1s are observed in Fig. 6d. One of the binding energies is 531.6 eV, which corresponds to O atoms related to oxygen vacancy, and the other is found to be 529.8 eV originating from lattice oxygen. Moreover, the typical ratio of the peak intensities for the O atoms related to oxygen vacancy and lattice oxygen increases obviously via adding sulfur source. Therefore, the O 1s XPS spectra can further announce that the concentration of oxygen vacancy increases in the process of forming heterojunction, which is consistent with the results of ESR spectra (Fig. 5a).

N_2 adsorption-desorption isotherm measurements are conducted in order to further investigate the Brunauer-Emmett-Teller (BET) specific surface areas of the materials. Fig. 7a shows the N_2 adsorption-desorption isotherms of pure In_2O_3 , In_2S_3 and $\text{In}_2\text{O}_3/\text{In}_2\text{S}_3$ (III) heterostructure. It can be observed that the surface area of $\text{In}_2\text{O}_3/\text{In}_2\text{S}_3$ (III) heterostructure is $78.47 \text{ m}^2 \cdot \text{g}^{-1}$, which is larger than pure In_2O_3 with $64.17 \text{ m}^2 \cdot \text{g}^{-1}$ of specific surface area. Nevertheless, when the quantity of TAA is 0.1 g, the obtained material possesses a decreased specific surface area ($27.51 \text{ m}^2 \cdot \text{g}^{-1}$), because the production of a large number

of In_2S_3 sheets results in the blockage of channels. Overall, photocatalysts with larger specific surface area can provide more reaction sites and consequently improve the properties of nitrogen fixation.

The recombination of photogenerated electrons and holes can give rise to the emission of light, i.e. photoluminescence (PL). It is well known that lower PL intensities may imply lower recombination efficiencies of photogenerated electrons and holes, which usually leads to higher photoreactivity. As shown in Fig. 7b, the contrast of the PL spectra for pure In_2O_3 and $\text{In}_2\text{O}_3/\text{In}_2\text{S}_3$ (I II III IV) heterostructures is reflected. The PL spectra for all samples exhibit outstanding emission band at $\sim 468 \text{ nm}$ with the excitation wavelength of 350 nm. The highest PL intensity originates from the pure In_2O_3 , indicating the lowest separation rate of photogenerated electron-hole in all samples. However, when adding sulfur source, the PL intensity of $\text{In}_2\text{O}_3/\text{In}_2\text{S}_3$ heterostructures decreased. As a result, the formation of heterojunction obviously improves the separation efficiency of photoinduced electron-hole pairs, thus improving the photocatalytic nitrogen fixation efficiency.

Moreover, the photoelectrochemical measurements are carried out in order to investigate the charge separation behaviors of the pure In_2O_3 , In_2S_3 and $\text{In}_2\text{O}_3/\text{In}_2\text{S}_3$ heterostructures. Firstly, the transient photocurrent response measurement with each switch-on and -off event under UV-vis light illumination can directly reflect the lifetime of photogenerated charge carriers and the separation efficiency of electron-hole pairs. As disclosed in Fig. 8a, the photocurrent densities of pure In_2O_3 and In_2S_3 are $0.1 \mu\text{A}/\text{cm}^2$ and $1.0 \mu\text{A}/\text{cm}^2$, respectively, which are lower than that of $\text{In}_2\text{O}_3/\text{In}_2\text{S}_3$ (I II III IV) heterostructures. In particular, it is worth to note that the $\text{In}_2\text{O}_3/\text{In}_2\text{S}_3$ (III) heterostructure possesses the highest photocurrent density about $2.5 \mu\text{A}/\text{cm}^2$. To further elucidate the effect of charge carrier transport behavior, the EIS plots of pure In_2O_3 , In_2S_3 and $\text{In}_2\text{O}_3/\text{In}_2\text{S}_3$ heterostructures (III) are measured. As shown in Fig. 8b, among the three samples, the arc radius of $\text{In}_2\text{O}_3/\text{In}_2\text{S}_3$ heterostructure (III) is the smallest one, suggesting its lowest resistance for interfacial charge transfer and effectively

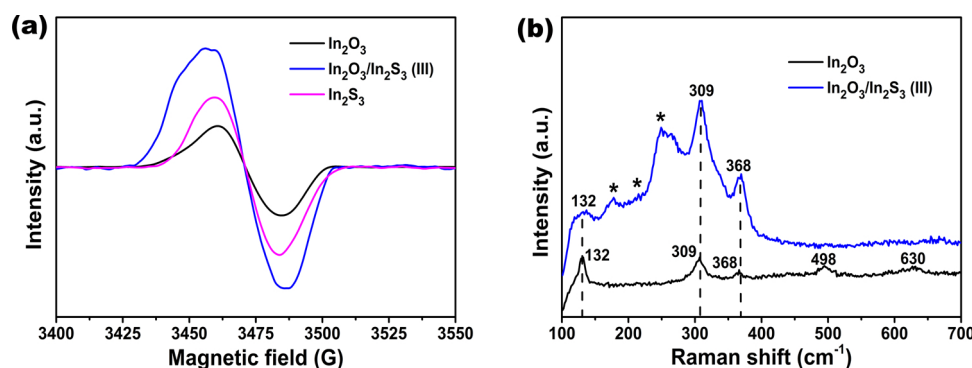


Fig. 5. (a) ESR spectra of pure In_2O_3 , $\text{In}_2\text{O}_3/\text{In}_2\text{S}_3$ (III) heterostructure and In_2S_3 . (b) Raman spectra depicting the characteristic vibrational modes of pure In_2O_3 , $\text{In}_2\text{O}_3/\text{In}_2\text{S}_3$ (III) heterostructure.

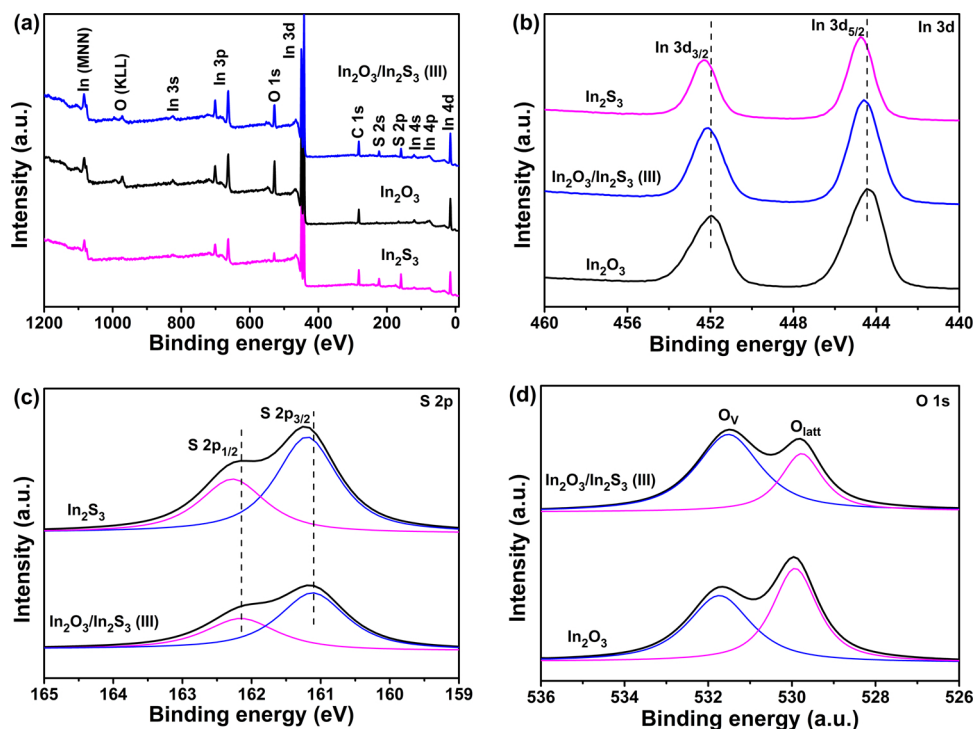


Fig. 6. High-resolution XPS spectra of as-prepared samples (a) Survey spectra of the pure In_2O_3 , $\text{In}_2\text{O}_3/\text{In}_2\text{S}_3$ (III) heterostructure and In_2S_3 samples. (b) In 3d. (c) S 2p and (d) O 1s.

separation of the photoinduced electron-hole pairs [45].

Mott-Schottky analysis is performed to figure out the band structure. Fig. 8c shows the Mott-Schottky plots of In_2O_3 and In_2S_3 samples. As can be seen from the results, the flat band potentials (E_{fb}) of In_2O_3 and In_2S_3 photocatalysts are calculated to be -0.83 and -0.72 eV vs. Ag/AgCl (or -0.63 and -0.52 eV vs. SHE), respectively. In addition, the slopes of the line show that In_2O_3 and In_2S_3 are n-type semiconductors. Conduction band potential (E_{CB}) is 0.1 V more negative than E_{fb} . Therefore, the E_{CB} values of In_2O_3 and In_2S_3 , estimated to be -0.73 and -0.62 eV vs. SHE, are more negative than the standard redox potential of N_2/NH_3 (-0.092 V vs. SHE).

3.2. Improved photocatalytic activity of $\text{In}_2\text{O}_3/\text{In}_2\text{S}_3$ microsphere heterostructures

3.2.1. Photocatalytic nitrogen fixation performance of $\text{In}_2\text{O}_3/\text{In}_2\text{S}_3$ microsphere heterostructures

All the as-prepared samples are subsequently evaluated for their ability to convert N_2 to NH_3 under UV-vis light irradiation by using N_2 -saturated water as the solvent and proton source. Quantitative

determination of NH_3 generation is conducted by spectrophotometrically measuring with Nessler's reagent. As shown in Fig. 9a, all of the samples generate a significant amount of NH_3 in the N_2 atmosphere after 2 h, and the concentration of NH_3 increases over time. The amount of generated NH_3 followed the order $\text{In}_2\text{O}_3/\text{In}_2\text{S}_3$ (III) heterostructure ($80.08 \mu\text{mol g}^{-1}$) > $\text{In}_2\text{O}_3/\text{In}_2\text{S}_3$ (IV) heterostructure ($58.40 \mu\text{mol g}^{-1}$) > $\text{In}_2\text{O}_3/\text{In}_2\text{S}_3$ (II) heterostructure ($40.04 \mu\text{mol g}^{-1}$) > $\text{In}_2\text{O}_3/\text{In}_2\text{S}_3$ (I) heterostructure ($26.70 \mu\text{mol g}^{-1}$) > pure In_2O_3 ($16.93 \mu\text{mol g}^{-1}$) > pure In_2S_3 ($13.38 \mu\text{mol g}^{-1}$). Furthermore, the rate of photocatalytic N_2 fixation is estimated to be as high as $40.04 \mu\text{mol g}^{-1} \text{h}^{-1}$ for the as-synthesized $\text{In}_2\text{O}_3/\text{In}_2\text{S}_3$ (III) heterostructure, which is 4.7 times higher than that of pure In_2O_3 and 6.0 times higher than that of pure In_2S_3 . In order to verify photocatalytic stability of $\text{In}_2\text{O}_3/\text{In}_2\text{S}_3$ (I II III IV) heterostructures, the cycle experiments are conducted, as shown in Fig. 9b. The $\text{In}_2\text{O}_3/\text{In}_2\text{S}_3$ (III) heterostructure also displays excellent photocatalytic stability with no obvious decrease in activity. Besides, for the further investigation of the stability of crystalline structure and morphology, the used materials are recovered to conduct the characterization of XRD and SEM, as shown in Fig. S1 and Fig. S2.

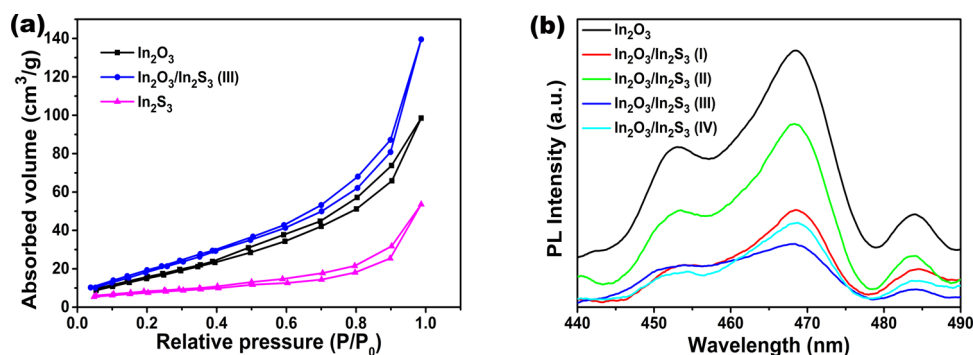


Fig. 7. (a) BET adsorption-desorption isotherms of pure In_2O_3 , $\text{In}_2\text{O}_3/\text{In}_2\text{S}_3$ (III) heterostructure and In_2S_3 . (b) PL spectra of pure In_2O_3 and $\text{In}_2\text{O}_3/\text{In}_2\text{S}_3$ (I II III IV) heterostructures.

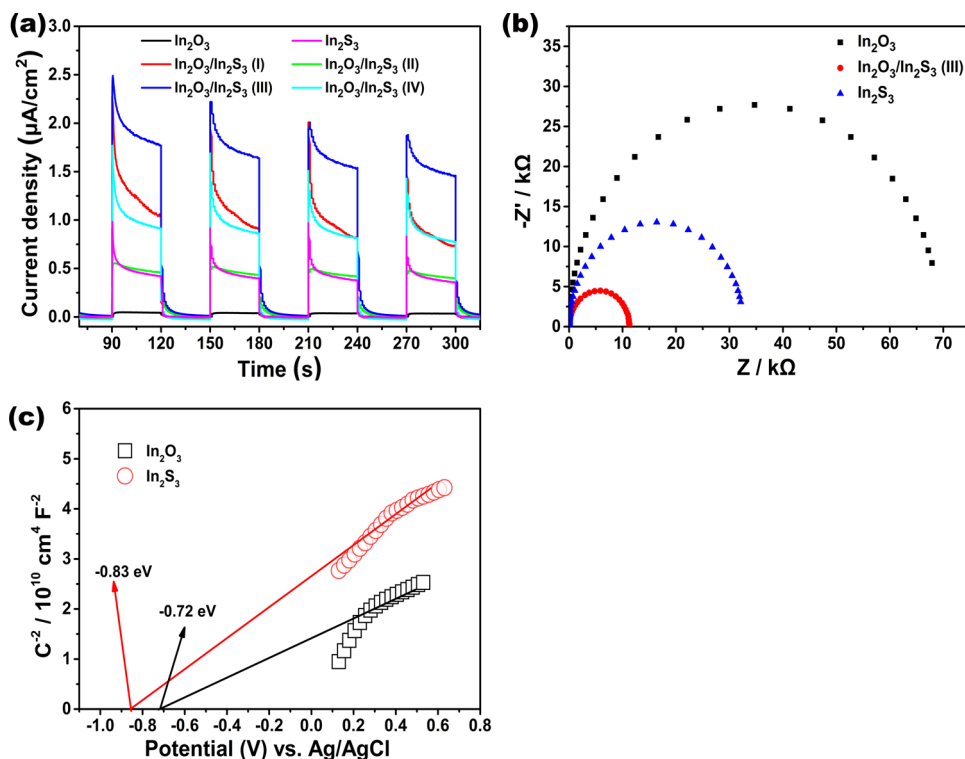


Fig. 8. (a) Transient photocurrent responses of pure In_2O_3 , In_2S_3 and $\text{In}_2\text{O}_3/\text{In}_2\text{S}_3$ (I II III IV) heterostructures. (b) EIS plots of pure In_2O_3 , In_2S_3 and $\text{In}_2\text{O}_3/\text{In}_2\text{S}_3$ (III) heterostructure. (c) Mott-schottky plots of pure In_2O_3 and In_2S_3 .

The results illustrate that no distinct change can be observed, thus the $\text{In}_2\text{O}_3/\text{In}_2\text{S}_3$ (III) possesses high stability. The control experiments are performed by using Ar as nitrogen source instead of N_2 , and the results are displayed in Fig. 9c. The sample shows the negligible NH_3 production, which clearly confirms that the N element generating ammonia come from N_2 . Then the experiment of N_2 fixation was conducted in dark, and Fig. 9d displayed that no trace of

NH_3 was detected during the process of N_2 fixation, which reveals the electron-donating nature of excited $\text{In}_2\text{O}_3/\text{In}_2\text{S}_3$ (III) heterostructure. As for the byproducts in the process of N_2 fixation, the amount of O_2 and NO_3^- can be detected by gas chromatography and ion chromatography, as displayed in Fig. S3.

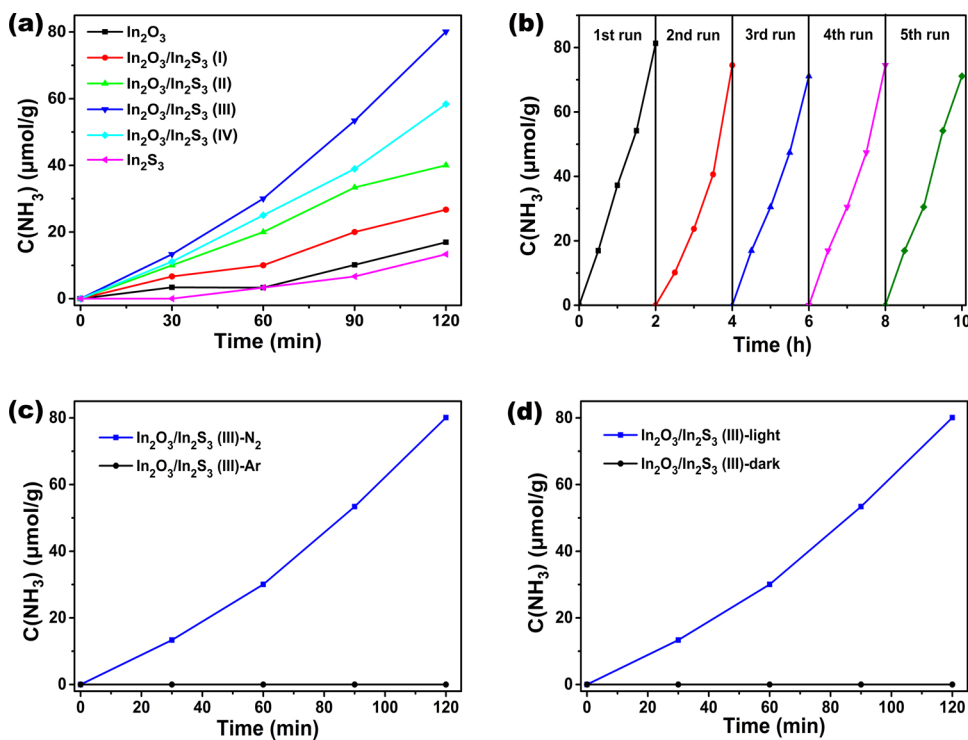
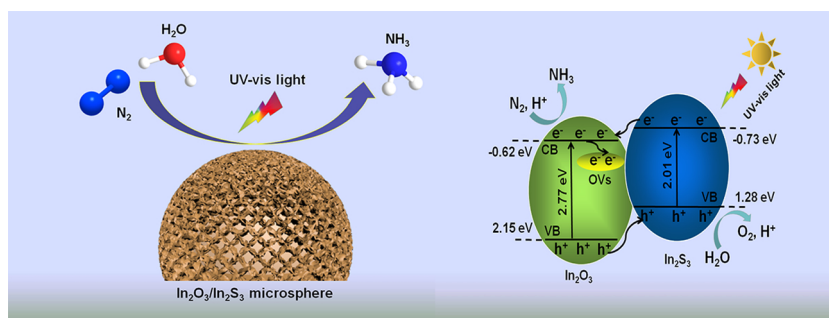


Fig. 9. (a) Quantitative determination of the generated NH_3 under UV-vis light. (b) Catalyst cycling tests for $\text{In}_2\text{O}_3/\text{In}_2\text{S}_3$ (III) heterostructure under N_2 in the water under UV-vis light. (c) Photocatalytic nitrogen fixation tests for $\text{In}_2\text{O}_3/\text{In}_2\text{S}_3$ (III) heterostructure under Ar in the water under UV-vis light. (d) Photocatalytic nitrogen fixation tests for $\text{In}_2\text{O}_3/\text{In}_2\text{S}_3$ (III) heterostructure under N_2 in the water in dark.



Scheme 2. Schematic illustration showing the mechanism for photocatalytic nitrogen fixation.

3.2.2. Mechanism of photocatalytic nitrogen fixation

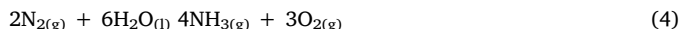
In order to study the photocatalytic reaction mechanism of $\text{In}_2\text{O}_3/\text{In}_2\text{S}_3$ heterojunctions, the valence band (VB) potentials of pure In_2O_3 and pure In_2S_3 can be theoretically calculated by Mulliken electro-negativity theory [46,47], the formula as following:

$$E_{\text{VB}} = X - E^{\text{e}} + 0.5E_{\text{g}} \quad (2)$$

where the E_{VB} is VB edge potential, X represents electro-negativity of the semiconductor material, the values of which for pure In_2O_3 and pure In_2S_3 are 5.28 and 4.76 eV respectively, and E^{e} is the energy of free electrons on the hydrogen scale (about 4.5 eV). According to the Eq. (2), the E_{VB} values of pure In_2O_3 and In_2S_3 are 2.16 and 1.17 eV, respectively. Moreover, the bandgap energy of semiconductor materials is shown in Fig. 4b. The conduction band (CB) edge potential (E_{CB}) can be obtained by Eq. (3), and the values of pure In_2O_3 and pure In_2S_3 are -0.59 and -0.75 eV, respectively, which are consistent with the results of Mott-Schottky analysis.

$$E_{\text{CB}} = E_{\text{VB}} - E_{\text{g}} \quad (3)$$

The mechanism of the enhancement in nitrogen fixation by $\text{In}_2\text{O}_3/\text{In}_2\text{S}_3$ heterostructures is further investigated via calculating the approximate band-edge positions relative to the reaction redox potentials. According to the calculation of band gap energy, the VB maximum of the pure In_2O_3 is 2.15 eV, more positive than that of In_2S_3 , whereas the CB minimum of the In_2S_3 is -0.73 eV, more negative than that of In_2O_3 . The schematic diagram is shown in Scheme 2, which indicates the illustration of charge separation and transfer pathway in $\text{In}_2\text{O}_3/\text{In}_2\text{S}_3$ heterostructures. Under irradiation, In_2O_3 and In_2S_3 can absorb the photons to induce lots of electrons and holes, and then the electrons in the VB of In_2S_3 migrate to the VB of In_2O_3 . At the same time, the holes transfer in the opposite direction. As a consequence, the photoexcited electrons and holes can be effectively separated in space. Subsequently, the stored electrons can react with the adsorbed N_2 molecules to generate NH_3 by selective reduction, and holes left on the VB oxidize H_2O into O_2 (Eq. (4)) [48].



Furthermore, according to results of the aforementioned ESR (Fig. 5a) and Raman (Fig. 5b), the trap states induced by oxygen vacancies can act as electron acceptor to promote the transfer of photo-induced electron. Therefore, the performance of photocatalytic nitrogen fixation of $\text{In}_2\text{O}_3/\text{In}_2\text{S}_3$ heterostructures can be improved.

4. Conclusion

In this work, $\text{In}_2\text{O}_3/\text{In}_2\text{S}_3$ heterostructures materials were fabricated by a simple two-step hydrothermal process and first applied to efficient fixation of N_2 to NH_3 under mild conditions. The In_2O_3 microsphere acts as host materials on which the In_2S_3 flakes are in situ generated and uniformly assembled when adding sulfur sources with different concentrations. Under UV-vis light irradiation, the photocatalytic

nitrogen fixation activity of the $\text{In}_2\text{O}_3/\text{In}_2\text{S}_3$ (III) heterostructure is significantly higher than that of pure In_2O_3 and In_2S_3 . The nitrogen fixation rate of $\text{In}_2\text{O}_3/\text{In}_2\text{S}_3$ (III) heterostructure is $40.04 \mu\text{mol g}^{-1} \text{h}^{-1}$, which is about 4.7 and 6.0 times higher than that of pure In_2O_3 and In_2S_3 , respectively. The enhanced photocatalytic nitrogen fixation is ascribed to the formation of heterostructures with the existence of oxygen vacancies, thus improving the separation of photogenerated electron-hole pairs and the utilization of photon of solar spectrum. Also, this work provides a new vista of the application of $\text{In}_2\text{O}_3/\text{In}_2\text{S}_3$ heterostructures in photocatalytic nitrogen fixation.

Declarations of interest

None.

Acknowledgments

This work was supported by the Natural Science Foundation of China (No. 21878031), Liaoning Province Natural Science Foundation (No. 20180550770) and LiaoNing Revitalization Talents Program (No. XLYC1802124).

Appendix A. Supplementary data

Supplementary material related to this article can be found, in the online version, at doi:<https://doi.org/10.1016/j.apcatb.2019.117932>.

References

- [1] H. Li, J. Shang, Z. Ai, L. Zhang, *J. Am. Chem. Soc.* 137 (2015) 6393–6399.
- [2] R. Lan, J.T.S. Irvine, S. Tao, *Int. J. Hydrogen Energy* 37 (2012) 1482–1494.
- [3] A. Klerke, C.H. Christensen, J.K. Nørskov, T. Vegge, *J. Mater. Chem.* 18 (2008) 2304–2310.
- [4] B.M. Hoffman, D. Lukoyanov, Z.-Y. Yang, D.R. Dean, L.C. Seefeldt, *Chem. Rev.* 114 (2014) 4041–4062.
- [5] T. Oshikiri, K. Ueno, H. Misawa, *Angew. Chemie Int. Ed.* 53 (2014) 9802–9805.
- [6] X. Du, J. Huang, Y. Feng, Y. Ding, *Chin. J. Catal.* 37 (2016) 123–134.
- [7] H.-P. Jia, E.A. Quadrelli, *Chem. Soc. Rev.* 43 (2014) 547–564.
- [8] A.E. Shilov, *Russ. Chem. Bull.* 52 (2003) 2555–2562.
- [9] X. Chen, N. Li, Z. Kong, W.-J. Ong, X. Zhao, *Mater. Horiz.* 5 (2018) 9–27.
- [10] H. Hirakawa, M. Hashimoto, Y. Shiraishi, T. Hirai, *J. Am. Chem. Soc.* 139 (2017) 10929–10936.
- [11] Y.T. Liang, B.K. Vijayan, K.A. Gray, M.C. Hersam, *Nano Lett.* 11 (2011) 2865–2870.
- [12] M.G. Walter, E.L. Warren, J.R. McKone, S.W. Boettcher, Q. Mi, E.A. Santori, N.S. Lewis, *Chem. Rev.* 110 (2010) 6446–6473.
- [13] P.J. Britto, K.S.V. Santhanam, P.M. Ajayan, *Bioelectrochem. Bioenerg.* 41 (1996) 121–125.
- [14] H. Yan, Y. Xie, Y. Jiao, A. Wu, C. Tian, X. Zhang, L. Wang, H. Fu, *Adv. Mater.* 30 (2018) 1704156.
- [15] S. Cao, H. Chen, F. Jiang, X. Wang, *Appl. Catal. B: Environ.* 224 (2018) 222–229.
- [16] N. Zhang, A. Jalil, D. Wu, S. Chen, Y. Liu, C. Gao, W. Ye, Z. Qi, H. Ju, C. Wang, X. Wu, L. Song, J. Zhu, Y. Xiong, *J. Am. Chem. Soc.* 140 (2018) 9434–9443.
- [17] Z. Wang, C. Hou, Q. De, F. Gu, D. Han, *ACS Sens.* 3 (2018) 468–475.
- [18] P. Rai, J.-W. Yoon, C.-H. Kwak, J.-H. Lee, *J. Mater. Chem. A* 4 (2016) 264–269.
- [19] F. Huang, W. Yang, F. He, S. Liu, *Sens. Actuators B Chem.* 235 (2016) 86–93.
- [20] L.-Y. Chen, W.-D. Zhang, *Appl. Surf. Sci.* 301 (2014) 428–435.
- [21] M. Meng, X. Wu, X. Zhu, L. Yang, Z. Gan, X. Zhu, L. Liu, P.K. Chu, *J. Phys. Chem. Lett.* 5 (2014) 4298–4304.

- [22] D. Wei, W. Jiang, H. Gao, X. Chuai, F. Liu, F. Liu, P. Sun, X. Liang, Y. Gao, X. Yan, G. Lu, *Sens. Actuators B Chem.* 276 (2018) 413–420.
- [23] S. Martha, K.H. Reddy, K.M. Parida, *J. Mater. Chem. A* 2 (2014) 3621–3631.
- [24] Q. Zhang, X. Li, Q. Zhao, Y. Shi, F. Zhang, B. Liu, J. Ke, L. Wang, *Appl. Surf. Sci.* 337 (2015) 27–32.
- [25] J. Mu, C. Shao, Z. Guo, M. Zhang, Z. Zhang, P. Zhang, B. Chen, Y. Liu, *J. Mater. Chem.* 22 (2012) 1786–1793.
- [26] S. Wang, B.Y. Guan, Y. Lu, X.W.D. Lou, *J. Am. Chem. Soc.* 139 (2017) 17305–17308.
- [27] Z. Li, Y. Dzenis, *Talanta* 85 (2011) 82–85.
- [28] X. Fu, X. Wang, Z. Chen, Z. Zhang, Z. Li, D.Y.C. Leung, L. Wu, X. Fu, *Appl. Catal. B: Environ.* 95 (2010) 393–399.
- [29] G. Liu, X. Jiao, Z. Qin, D. Chen, *CrystEngComm* 13 (2011) 182–187.
- [30] X. An, J.C. Yu, F. Wang, C. Li, Y. Li, *Appl. Catal. B: Environ.* 129 (2013) 80–88.
- [31] Y.H. Kim, J.H. Lee, D.-W. Shin, S.M. Park, J.S. Moon, J.G. Nam, J.-B. Yoo, *Chem. Commun.* 46 (2010) 2292–2294.
- [32] W. Qiu, M. Xu, X. Yang, F. Chen, Y. Nan, J. Zhang, H. Iwai, H. Chen, *J. Mater. Chem.* 21 (2011) 13327–13333.
- [33] J. Hou, S. Cao, Y. Sun, Y. Wu, F. Liang, Z. Lin, L. Sun, *Adv. Energy Mater.* 8 (2018) 1701114.
- [34] X. Yang, J. Xu, T. Wong, Q. Yang, C.-S. Lee, *Phys. Chem. Chem. Phys.* 15 (2013) 12688–12693.
- [35] F. Zhang, X. Li, Q. Zhao, A. Chen, *J. Phys. Chem. C* 120 (2016) 19113–19123.
- [36] S.-W. Cao, X.-F. Liu, Y.-P. Yuan, Z.-Y. Zhang, Y.-S. Liao, J. Fang, S.C.J. Loo, T.C. Sum, C. Xue, *Appl. Catal. B: Environ.* 147 (2014) 940–946.
- [37] G.K. Pradhan, D.K. Padhi, K.M. Parida, *ACS Appl. Mater. Interfaces* 5 (2013) 9101–9110.
- [38] F. Zhang, X. Li, Q. Zhao, Q. Zhang, M. Tadó, S. Liu, *J. Colloid Interface Sci.* 457 (2015) 18–26.
- [39] Y. Jia, D. Zhao, M. Li, H. Han, C. Li, *Chin. J. Catal.* 39 (2018) 421–430.
- [40] Y. Jiang, H. Ning, C. Tian, B. Jiang, Q. Li, H. Yan, X. Zhang, J. Wang, L. Jing, H. Fu, *Appl. Catal. B: Environ.* 229 (2018) 1–7.
- [41] F. Lei, Y. Sun, K. Liu, S. Gao, L. Liang, B. Pan, Y. Xie, *J. Am. Chem. Soc.* 136 (2014) 6826–6829.
- [42] J. Gan, X. Lu, J. Wu, S. Xie, T. Zhai, M. Yu, Z. Zhang, Y. Mao, S.C.I. Wang, Y. Shen, Y. Tong, *Sci. Rep.* 3 (2013) 1021.
- [43] H. Li, J. Li, Z. Ai, F. Jia, L. Zhang, *Angew. Chem. Int. Ed.* 57 (2018) 122–138.
- [44] M. Kaur, N. Jain, K. Sharma, S. Bhattacharya, M. Roy, A.K. Tyagi, S.K. Gupta, J.V. Yakhmi, *Sens. Actuators B Chem.* 133 (2008) 456–461.
- [45] B. Zhang, L. Wang, Y. Zhang, Y. Ding, Y. Bi, *Angew. Chem. Int. Ed.* 57 (2018) 2248–2252.
- [46] J. Zhang, J. Lv, K. Dai, C. Liang, Q. Liu, *Appl. Surf. Sci.* 430 (2018) 639–646.
- [47] J. Jin, J. Yu, D. Guo, C. Cui, W. Ho, *Small* 11 (2015) 5262–5271.
- [48] S. Sun, X. Li, W. Wang, L. Zhang, X. Sun, *Appl. Catal. B: Environ.* 200 (2017) 323–329.